



# Local dynamics of a randomly pinned crack front: a numerical study

Knut S. Gjerden, Arne Stormo and Alex Hansen\*

Department of Physics, Norwegian University of Science and Technology (NTNU), Trondheim, Norway

## Edited by:

José S. Andrade Jr., Universidade Federal do Ceará, Brazil

## Reviewed by:

Haroldo Valentin Ribeiro, Universidade Estadual de Maringá, Brazil

Nuno A. M. Araújo, Universidade de Lisboa, Portugal

## \*Correspondence:

Alex Hansen, Department of Physics, Norwegian University of Science and Technology (NTNU), Høyskoleringen 5, NO-7491 Trondheim, Norway  
e-mail: alex.hansen@ntnu.no

We investigate numerically the dynamics of crack propagation along a weak plane using a model consisting of fibers connecting a soft and a hard clamp. This bottom-up model has previously been shown to contain the competition of two crack propagation mechanisms: coalescence of damage with the front on small scales and pinned elastic line motion on large scales. We investigate the dynamical scaling properties of the model, both on small and large scale. The model results compare favorably with experimental results on stable crack propagation between sintered PMMA plates.

**Keywords:** fracture, dynamical critical phenomena, crackling phenomena, fracture roughness, avalanche dynamics

## 1. INTRODUCTION

The motion of a fracture front through a disordered medium is for obvious reasons of great practical importance. Nevertheless, it is a very complex problem which has kept material scientists and mechanical engineers occupied for almost two centuries [1]. In an attempt to simplify the problem, Schmittbuhl et al. [2] proposed to study the motion of a fracture front moving along a weak plane, thereby suppressing the out of plane motion of the front. In a seminal experimental study, Schmittbuhl and Måløy [3] followed this idea up by sintering two sandblasted plexiglass plates together and then plying them apart from one edge. The sintering made the otherwise due to the sandblasting, opaque plates transparent. Where the plates were broken apart again, the opaqueness returned. Hence, it was possible to identify and follow the motion of the front since the plates would be transparent in front of the crack front and opaque behind it. There have been a large number of studies on this system following this initial work. Most of these studies have been theoretical or numerical in character and they have mostly dealt with the roughness of the crack front, see e.g., Ramanathan et al. [4], Delaplace et al. [5], Rosso and Krauth [6] Schmittbuhl et al. [7] and Santucci et al. [8]. See also the recent reviews by Bonamy [9] and Bonamy and Bouchaud [10].

The roughness is only one aspect of the motion of the crack front in this system. A first study of the dynamics of the front was published by Måløy and Schmittbuhl in 2001 [11]. The velocity distribution was measured and found to decay slower than an exponential. This was followed by a study by Måløy et al. [12] introducing the waiting time matrix technique making it possible to measure pixel by pixel the time the front sits still locally. This revealed an avalanche structure where portions of the front would sweep an area  $S$  with a velocity  $v$  before halting again. Both the distribution of areas and velocities were power laws. In two

later papers, Tallakstad et al. [13] and Lengliné et al. [14], have continued and refined this work.

The fluctuating line model, based on the idea that the crack front moves as a pinned elastic line [2, 15], dominates the theoretical descriptions of the constrained crack problem. It is a top-down approach where the motion of the crack front is derived from continuum elastic theory. Its earliest use was to calculate the roughness exponent controlling the scaling properties of the crack front. If  $h(x, t)$  is the position of the crack front at time  $t$  and position  $x$  along its base line, then one finds the height-height correlation function  $\langle (h(x + \Delta x) - h(x))^2 \rangle$  scaling as  $|\Delta x|^{2\zeta}$  where  $\zeta$  is the roughness exponent [2]. The most precise measurement of the roughness exponent with the fluctuating line model to date is  $\zeta = 0.388 \pm 0.002$  [6]. However, the experimental measurements of  $\zeta$  gave systematically a much larger value, namely around 0.6—Schmittbuhl and Måløy [3] found  $\zeta = 0.55 \pm 0.05$  and Delaplace et al. [5]  $\zeta = 0.63 \pm 0.03$ .

Santucci et al. [8] have reanalyzed data from a number of earlier studies, including Delaplace et al. [5], finding that the crack front has *two scaling regimes*: one small-scale regime described by a roughness exponent  $\zeta_- = 0.60 \pm 0.05$  and a large-scale regime described by a roughness exponent  $\zeta_+ = 0.35 \pm 0.05$ . Hence, there is a large scale roughness regime which is consistent with the fluctuating line model. However, the small scale regime is too rough.

Laurson et al. [16] has linked this regime to correlations in the pinning strength below the Larkin length within the fluctuating line model. This approach assumes that the physics behind both scaling regimes is describable within the same top-down model. Bonamy et al. [17] and Laurson et al. [16] have considered the crackling dynamics [18] of the fluctuating line model finding behavior consistent with the experimental measurements [11–14].

A very different approach to explain the roughness of the crack front has been proposed by Schmittbuhl et al. [7]. It is a bottom-up approach based on a stress-weighted gradient percolation process. This idea in turn has its origin in the proposal by Bouchaud et al. [19] that the crack front does not advance not only due to a competition between effective elastic forces and pinning forces at the front, but also by *coalescence* of damage in front of the crack with the advancing crack itself.

By refining the model proposed by Batrouni et al. [20] and Gjerden et al. [21], consisting of fibers clamped between a hard and a soft block and with a gradient in the breaking thresholds, we have identified two scaling regimes for the roughness of the advancing crack front [22]. On large scales we recover the roughness seen in the reanalysis of experimental data by Santucci et al. [8],  $\zeta_+ = 0.39 \pm 0.04$ , consistent with the fluctuating line model. On small scales, where the front advances mainly due to damage coalescence, we find the growth to be consistent with gradient percolation [23, 24]. As was shown by Hansen et al. [25], this implies a roughness exponent  $\zeta_- = 2/3$ . This value is consistent with the reanalysis of Santucci et al. [8].

We study in this paper the crackling dynamics in the fiber bundle model [20–22]. We find quantitative consistency with the experimental measurements. Hence, we demonstrate that this simple model contains the observed experimental features of constrained crack growth. It contains the essential physics of the problem. Since we have control over the crossover length scale between the crack advancing due to crack coalescence and due to pinning of the crack front as an elastic line, we analyse our results in light of this.

In Section 2, we describe the model in detail. Section 3.1 continues the analysis from Gjerden et al. [22] of the roughness of the crack front. In Gjerden et al. [22], we measured the roughness locally using the average wavelet coefficient method [26, 27]. Here we base our analysis on the variance of the front, again finding two regimes: a small-scale regime consistent with ordinary gradient percolation and a large-scale regime consistent with the fluctuating line model. In Section 3.2 we examine the velocity distribution during the motion of the crack front. Our data are consistent with the findings of Måløy et al. [12] and Tallakstad et al. [13]. Section 3.3 is devoted to an analysis of the geometry of the avalanches that occur during the motion of the crack front. The last section before the conclusion, Section 4 contains a tying up of loose ends through a discussion of the results.

The main aim of this paper has been to demonstrate that the simple model we use is capable of reproducing the experimental data. Hence, this simple fiber bundle model seems to contain the essential physics of the constrained crack problem.

## 2. MODEL AND METHOD

The model we base our calculations on is a refinement of the fiber bundle model [28] used by Schmittbuhl et al. [7] and introduced by Batrouni et al. the year before [20]. We illustrate the model in **Figure 1**.  $L \times L$  elastic fibers are placed in a square lattice between two parallel clamps. One of the clamps is infinitely stiff whereas the other has a finite Young modulus  $E$  and a Poisson ratio  $\nu$ . All fibers are equally long and have the same elastic constant  $k$ .

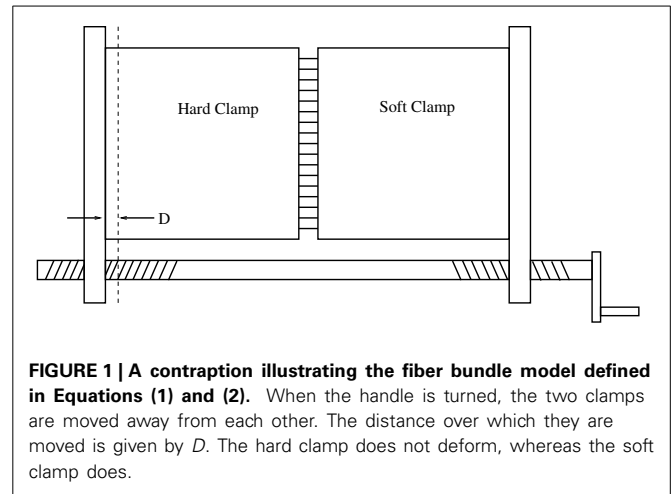


**FIGURE 1 | A contraption illustrating the fiber bundle model defined in Equations (1) and (2).** When the handle is turned, the two clamps are moved away from each other. The distance over which they are moved is given by  $D$ . The hard clamp does not deform, whereas the soft clamp does.

We measure the position of the stiff clamp with respect to its position when all fibers carry zero force,  $D$ , see **Figure 1**. The force carried by the fiber at position  $(i, j)$ , where  $i$  and  $j$  are coordinates in a cartesian coordinate system oriented along the two planes on which the fibers are clamped, is then

$$f_{(i,j)} = -k(u_{(i,j)} - D), \quad (1)$$

where  $u_{(i,j)}$  is the elongation of the fiber at  $(i, j)$ .

The fibers redistribute the forces they carry through the response of the soft clamp. The redistribution of forces is accomplished by using the Green function connecting the force  $f_{(m,n)}$  acting on the clamp from fiber  $(m, n)$  with the deformation  $u_{(i,j)}$  at fiber  $(i, j)$ , [29]

$$u_{(i,j)} = \sum_{(m,n)} G_{(i,j),(m,n)} f_{(m,n)}, \quad (2a)$$

$$G_{(i,j),(m,n)} = \frac{1 - \nu^2}{\pi E a^2} \int_{-a/2}^{a/2} dx \int_{-a/2}^{a/2} dy \frac{1}{|\vec{r}_{(i,j)} - \vec{r}_{(m+x,n+y)}|}. \quad (2b)$$

where  $a$  is the distance between neighboring fibers. The integration in Equation (2b) is performed over the Voronoi cell around each fiber.  $\vec{r}_{(i,j)}$  is the position of fiber  $(i, j)$ .  $\vec{r}_{(m+x,n+y)}$  is the position of a point  $(x, y)$  in the Voronoi cell surrounding the fiber at  $(m, n)$ .

The equation set, Equations (2) and (2b), is solved using a Fourier accelerated conjugate gradient method [30, 31].

The Green function, Equation (2b), is proportional to  $(Ea)^{-1}$ . The elastic constant of the fibers,  $k$ , must be proportional to  $a^2$ . The linear size of the system is  $aL$ . Hence, by changing the linear size of the system without changing the discretization  $a$ , we change  $L \rightarrow \lambda L$  but leave  $(Ea)$  and  $k$  unchanged. If we on the other hand change the discretization without changing the linear size of the system, we simultaneously set  $L \rightarrow \lambda L$ ,  $(Ea) \rightarrow \lambda(Ea)$  and  $k \rightarrow k/\lambda^2$ . Based on these observations, we define a scaled Young modulus

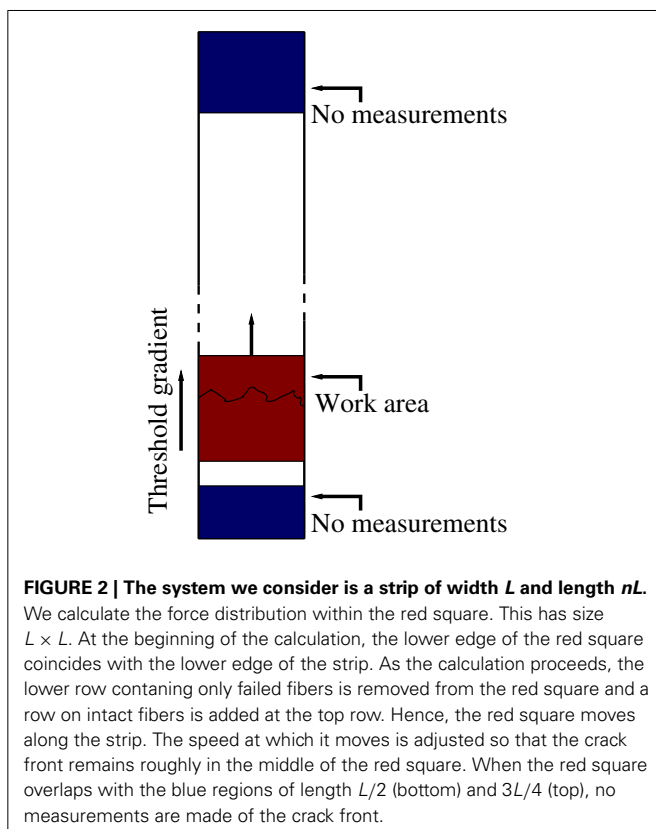
$$e = \frac{Ea}{L}. \quad (3)$$

Hence, changing  $e$  without changing  $k$  is equivalent to changing  $L$ —and hence the linear size of the system—while keeping the elastic properties of the system constant [32]. This is a central point in what follows.

The fibers are broken by using the quasistatic approach [33]. That is, we assign to each fiber  $(i, j)$  a threshold value  $t_{(i,j)}$ . They are then broken one by one by identifying the fiber which satisfies  $\max_{(i,j)} (f_{(i,j)}/t_{(i,j)})$  when the forces  $f_{i,j}$  have been calculated for  $D = 1$ . This ratio is then equal to  $1/D$  where  $D$  is the value at which the fiber fails.

In the constrained crack growth experiments of Schmittbuhl and Måløy [3], the two sintered plexiglass plates were plied apart from one edge. In the numerical modeling of Schmittbuhl et al. [7], an asymmetric loading was accomplished by introducing a linear gradient in  $D$ . Rather than implementing an asymmetric loading, we use here a gradient in the threshold distribution,  $t_{(i,j)} = gj + r_{(i,j)}$ , where  $g$  is the gradient and  $r_{(i,j)}$  is a random number drawn from a flat distribution on the unit interval.

In order to follow the crack front as the breakdown process develops, we implement the “conveyor belt” technique [21, 34]. We illustrate this technique in **Figure 2**. Fiber bundle forms a rectangle of width  $L$  and length  $nL$ , where  $n > 1$ . However, we do not consider all fibers at once, but a square of size  $L \times L$ . This is the red square in the figure. The square is initially placed at the bottom of the  $L \times nL$  strip and at regular intervals, the bottom row



in the square is removed and a new intact row is added at the top. In this way, the square moves along the strip, eventually passing from the bottom to the top. The speed at which the square moves is adjusted so that the crack front, shown as a black rough curve in the figure, stays roughly in the middle of the red square.

Only after the square has passed the  $L/2$  first rows (marked in blue in **Figure 2**) do we record the position of the front. This is to ensure that the front has entered a steady-state regime. We also do not record whence the red square is at a distance  $3L/4$  from the top. This is indicated as the blue region at the top of the figure. This is done to avoid boundary effects at this edge.

### 3. RESULTS

#### 3.1. ROUGHNESS AND DYNAMICAL SCALING

In Gjerden et al. [22], we presented evidence for two scaling regimes in the model we study here. For small values of the scaled elastic constant  $e$ —or equivalently large length scales—we found a roughness exponent  $\zeta_+ = 0.39 \pm 0.04$ , which is consistent with the fluctuating line model. On small scale, we found that the roughness exponent  $\zeta_-$  was consistent with the value  $2/3$ , the value expected in gradient percolation [25]. However, at these small scales, the fracture is fractal and we determined its fractal dimension to be  $1.77 \pm 0.02$ , which is consistent with that of the percolation hull,  $7/4$  [24].

We note in this connection that in the limit of completely stiff clamps, the system becomes equivalent to gradient percolation [23, 24]. Our statement on the small scale behavior of the soft clamp fiber bundle model is then that it is in the percolation universality class even though the clamps are not stiff.

In this section, we present further results concerning the existence of two scaling regimes in the soft clamp fiber bundle model beyond those that were presented in Gjerden et al. [22].

We identify the crack front by first eliminating all islands of surviving fibers behind it and all islands of failed fibers in front of it. We measure “time”  $n$  in terms of the number of failed fibers. After an initial period, the system settles into a steady state. We then record the position of the crack front  $j = j(i, n = 0)$  after having set  $n = 0$ . We then define the position at later times  $n > 0$  relative to this initial position,

$$h_i(n) = j(i, n) - j(i, n = 0). \quad (4)$$

This is the same definition as was used by Schmittbuhl and Måløy in their experimental studies [3]. The front as it has now been defined will contain overhangs. That is, there may be multiple values of  $h_i(n)$  for the same  $i$  and  $n$  values. We only keep the largest  $h_i(n)$ , i.e., we implement the Solid-on-Solid (SOS) front.

We define the average position of the front as

$$\langle h(n) \rangle = \frac{1}{L} \sum_{i=1}^L h_i(n), \quad (5)$$

and the front width as

$$w(n)^2 = \frac{1}{L} \sum_{i=1}^L (h_i(n) - \langle h(n) \rangle)^2. \quad (6)$$

We assume that  $\langle h \rangle$  grows linearly with the number of broken fibers  $n$ ,  $\langle h \rangle \propto n$ . In the following, we measure time in terms of  $\langle h \rangle$  rather than  $n$ .

### 3.1.1. Small scales

We now set  $e = 3.1$ . This places us in the regime that was identified in Gjerden et al. [22] as the small scale one. Here the fracture front has the fractal properties of the percolation hull. In Gjerden et al. [22], we used the averaged wavelet coefficient method to measure  $\zeta_-$ . In **Figure 3**, we show the width  $w$ , defined in Equation (6) as a function of  $\langle h \rangle$ . When  $w$  is rescaled as  $w/g_-^{\alpha_-}$  and  $\langle h \rangle$  as  $\langle h \rangle/g_-^{\beta_-}$ , we find data collapse for different values of the threshold gradient  $g$ . Hence, we have

$$w(\langle h \rangle, g) = g_-^{\alpha_-} \omega_- \left( \frac{\langle h \rangle}{g_-^{\beta_-}} \right), \quad (7)$$

where  $\omega_-$  is a scaling function given by

$$\omega_-(q) = \begin{cases} q^{\delta_-} & \text{if } q \rightarrow 0, \\ \text{constant} & \text{if } q \rightarrow \infty. \end{cases} \quad (8)$$

Hence, the front width saturates as  $\langle h \rangle$  grows beyond a given scale. Furthermore, we assume that  $w \sim \langle h \rangle^{\delta_-}$  for  $\langle h \rangle$  much smaller than this scale. We will determine  $\delta_-$  in a moment. Assuming the percolation universality class on small scales, we expect the two scaling exponents  $\alpha_-$  and  $\beta_-$  to obey the relation  $\alpha_- = \beta_- = \nu(1 + \nu) = 4/7$ , where  $\nu = 4/3$ , the percolation value. The derivation of the relations between  $\alpha_-$ ,  $\beta_-$  and  $\nu$  is given in Hansen et al. [25].

We now derive the value of  $\delta_-$  by relating  $\langle h \rangle$  to the number of fibers below and including the front,  $A$ , by the fractal dimension  $D_A = 91/48$  [35],  $\langle h \rangle^{D_A} \sim A$ . Invoking Mandelbrot's area-perimeter relation, we may also relate the length of the

front,  $l$  to the number of fibers below and including the front,  $l \sim A^{D_h/2}$ , where  $D_h = 7/4$  [24, 37]. Eliminating  $A$  between these two expressions leads to  $l \sim \langle h \rangle^{D_H D_A/2}$ . We relate the length of the front  $l$  to its width  $w$  by the relation  $l \sim w^{D_H} (L/w)$  [22]. Eliminating  $l$  between these two relations gives

$$w \sim \langle h \rangle^{\delta_-} = \langle h \rangle^{D_A D_H / (2 D_H - 2)} = \langle h \rangle^{288/637}. \quad (9)$$

Hence, we have that

$$\delta_- = \frac{288}{637} \approx 0.45. \quad (10)$$

The straight line in **Figure 3** has this slope.

By invoking Family-Vicsek scaling [36], a dynamical exponent  $\kappa_-$  may be defined. By setting  $W$  to be the width of the system in the  $x$  direction, i.e., orthogonally to the direction of the gradient, Family-Vicsek scaling takes the form

$$w(W, \langle h \rangle) = W^{\zeta_-} f_- \left( \frac{\langle h \rangle}{W^{\kappa_-}} \right), \quad (11)$$

where

$$f_-(q) = \begin{cases} q^{\zeta_-/\kappa_-} & \text{if } q \rightarrow 0, \\ \text{constant} & \text{if } q \rightarrow \infty. \end{cases} \quad (12)$$

We are here keeping the gradient  $g$  constant. Since the behavior of the Family-vicsek scaling function  $f$  must be the same as the one defined in Equation (8), we find the relation

$$\frac{\zeta_-}{\kappa_-} = \delta_-, \quad (13)$$

leading to

$$\kappa_- = \frac{637}{432} \approx 1.47. \quad (14)$$

### 3.1.2. Large scales

**Figure 4** shows the corresponding one-parameter scaling as in **Figure 3**, but now for systems with a much lower  $e = 7.8 \times 10^{-4}$ , placing us in the realm of the fluctuating line model [22]. We define as for the small scale study scaling relations Equations (7), (8), (11), and (12) corresponding relation, but where “-” has been exchanged for “+.”

The two scaling exponents that produce data collapse are  $\alpha_+ = \beta_+ = 0.4$ . By a least squares fit, we determine

$$w \sim \langle h \rangle^{\delta_+} = \langle h \rangle^{0.52 \pm 0.05}. \quad (15)$$

This value is very close to the one seen for large  $e$  values, and consistent with the experimental measurement of Tallakstad et al. [13], who found 0.55 and Schmittbuhl et al. [38] who found 0.52.

By invoking Family-Vicsek scaling as for the small-scale case, we may determine the dynamical exponent

$$\frac{\zeta_+}{\kappa_+} = \delta_+, \quad (16)$$

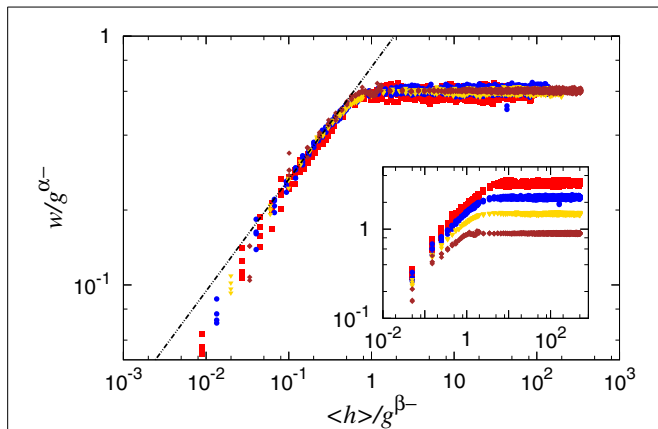


**FIGURE 3 | One-parameter scaling of the SD of the width of the front as a function of the average position of the front as the front moves forward from some initial (rough) configuration.** The main figure shows data collapse for  $\alpha_- = \beta_- = 4/7$ , and the inset shows the same data without rescaling. The straight line has slope  $288/637 \approx 0.45$ —see text. The data are extracted from simulations with, from top-down in the inset,  $g \in (0.05, 0.1, 0.2, 0.5)$ . Each data set is based on 100 samples for  $L = 64$  and  $n = 5$ , 10 samples for  $L = 128$  and  $n = 5$ , and 10 samples for  $L = 256$  and  $n = 2$ .

so that  $\kappa_+ = 0.75 \pm 0.07$ . This is consistent with the value reported by Duemmer and Krauth for the fluctuating line model,  $\kappa = 0.770 \pm 0.005$  [39].

The dynamical exponent reported by Måløy and Schmittbuhl [11] for the PMMA system was  $\kappa = 1.2$ . This value sits between the values we find for  $\kappa_-$  and  $\kappa_+$ .

### 3.1.3. Height fluctuations

It was observed by Santucci et al. [8] that the large-scale roughness regime shows a gaussian distribution of the height fluctuations,

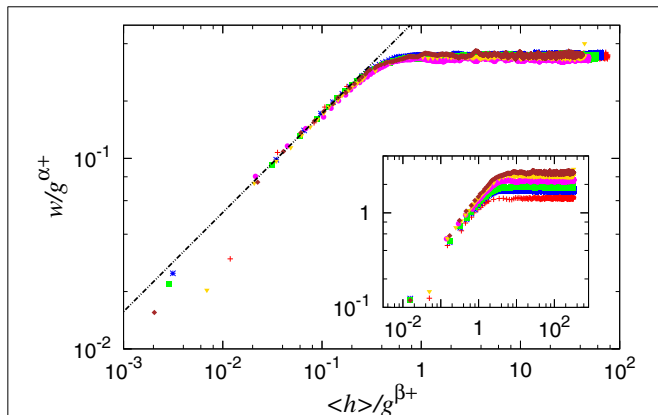


**FIGURE 4 | One-parameter scaling of  $w$  as a function of  $\langle h \rangle$  with  $g$  as the scaling parameter.** The main figure shows data collapse for  $\alpha_+ = \beta_+ = 0.4$ . The inset shows unscaled data. The slope of the straight line is 0.52. The parameter values are, from top-down in the inset,  $g \in (0.007, 0.008, 0.01, 0.015, 0.02, 0.03)$ . The data sets are based on 200–800 samples for  $L = 64$  and  $n = 10$ .

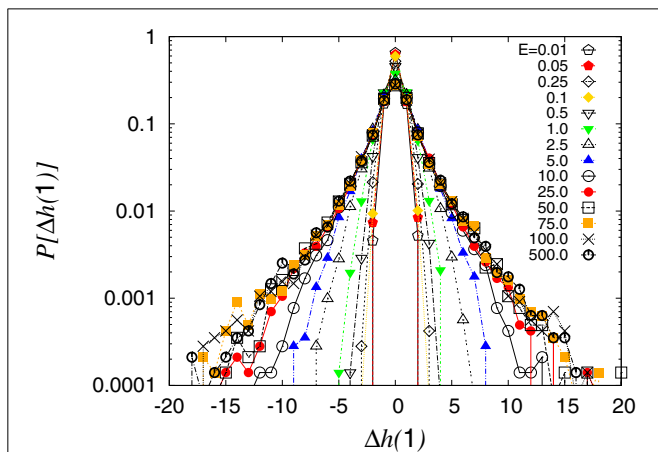


**FIGURE 5 | Histogram of height fluctuations with respect to  $\Delta h(1) = |h_{i+1}(n) - h_i(n)|$  for different elastic constants.** The distribution follows a gaussian when the system is soft and broadens when the system stiffens. This is equivalent to changing the step size between measurements of the crack front, as was done in Santucci et al. [8]. These measurements are based on a single strip of with  $L = 128$ , and length  $nL = 10 \times 128$ . The data were recorded when the front was at 112 different positions, spaced so far apart that they were statistically independent.

whereas in the small-scale it broadens to a non-gaussian distribution, see Figure 3 in Santucci et al. We investigate this in our model. We define the height fluctuations as  $\Delta h(1) = |h_{i+1}(n) - h_i(n)|$ . By changing the elastic constant,  $L$  in our model while keeping the step size constant, the result is equivalent to changing the step size in the experiment, where they measured  $|h(x + \delta) - h(x)|$  for different values of  $\delta$ . We show in **Figure 5** the distribution of fluctuations for different elastic constant  $E$ . We observe that for soft systems, the distribution is gaussian (i.e., follows a parabola in the plot). As the system stiffens, the distribution broadens.

## 3.2. LOCAL VELOCITY DISTRIBUTION

We examine the distribution of local velocities using the Waiting Time Matrix (WTM) method [12]. The WTM method consists of letting the fracture move across a matrix with all elements initially equal to zero in discrete time steps. At every time step, the matrix elements containing the front are incremented by one. When the front has passed, the matrix contains the time the front spent in each position measured in time steps. Hence, matrix elements containing low values correspond to rapid front movements and large values correspond to slow, pinned movement. One may then calculate the spatiotemporal map of velocities,  $v(x, y)$ , by inverting the waiting time recorded in each matrix element. From this map we then calculate the global average velocity  $\langle v \rangle$  and the distribution of local velocities  $P(v)$ . Tallakstad et al. find experimentally that this distribution follows a power law,

$$P(v/\langle v \rangle) \sim (v/\langle v \rangle)^{-\eta}, \quad \text{for } v/\langle v \rangle > 1, \quad (17)$$

with the exponent  $\eta = 2.55 \pm 0.15$  [12, 13].

The results from our simulations are shown in **Figure 6** for scaled elastic constant  $e = 1.6 \times 10^{-4}$  and  $7.8 \times 10^{-4}$ , which places us in the large-scale regime. We use these values for  $e$  throughout this section unless explicitly stated otherwise. The slope in the figure is obtained through a linear fit and has the value  $\eta_+ = 2.53$ , where the subscript “+” indicates that this is in the large-scale regime.

The data in this section is based on systems of width  $L = 64$  and length  $nL = 5 \times 64$  or  $L = 128$  and  $nL = 2 \times 128$ . The waiting time matrix was calculated from 15460 ( $L = 64$ ) or 12288 ( $L = 128$ ) snapshots of the front position.

### 3.2.1. Space and time correlations

From the local velocities, still in the large-scale regime, we calculate the normalized correlation functions in space,  $G(\Delta x)$ , and time,  $G(\Delta t)$

$$G(\Delta x) = \left\langle \frac{[v(x + \Delta x, t) - \langle v \rangle_x][v(x, t) - \langle v \rangle_x]}{\sigma_x^2} \right\rangle_t, \quad (18a)$$

$$G(\Delta t) = \left\langle \frac{[v(x, t + \Delta t) - \langle v \rangle_t][v(x, t) - \langle v \rangle_t]}{\sigma_t^2} \right\rangle_x. \quad (18b)$$

$\sigma_{x/t}$  and  $\langle \rangle_{x/t}$  denote standard deviation and average over  $x$  or  $t$ .

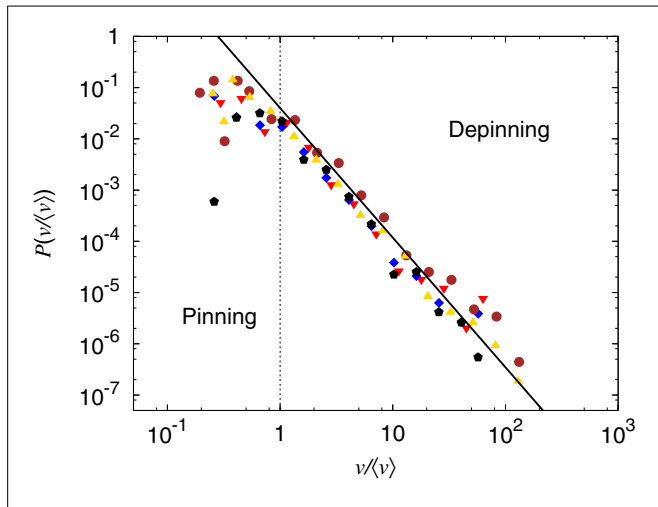


**FIGURE 6 | Distribution of local velocities scaled by the global average velocity.** Results are based on simulations of sizes  $L = 64, 128$  with  $e = 1.56 \times 10^{-4}, 7.81 \times 10^{-4}$ , respectively, and loading gradient in the range  $g \in [0.01 - 0.05]$ . A fit to the data for  $v > \langle v \rangle$  yields a power law behavior with an exponent of  $-2.53$ . The values of  $e$  correspond to the fluctuating line regime.

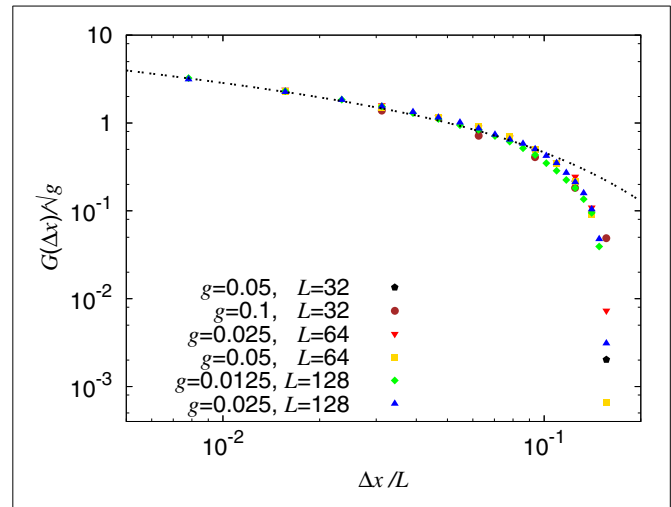


**FIGURE 7 | Spatial correlation function  $G(\Delta x)$ .** Data collapse is obtained when  $\Delta x$  is scaled with the system size and  $G(\Delta x)$  is scaled with  $\sqrt{g}$ . The line is a fit to a power law with exponential cutoff  $G(\Delta x) = A(\Delta x/L)^{-0.4} \exp(-\Delta x/0.1L)$ . The system sizes and elastic constant used are as in **Figure 6**.

The results for  $G(\Delta x)$  are presented in **Figure 7**, where we fit the data to the function

$$G(\Delta x) = A \left( \frac{\Delta x}{x^*} \right)^{-\tau_x} \exp \left( -\frac{\Delta x}{x^*} \right), \quad (19)$$

where  $x^* = 0.1L$  and  $\tau_x = 0.4$ . This functional form was proposed by Tallakstad et al. [13] with  $\tau_x = 0.53 \pm 0.12$ . We note that the cutoff in our data is much sharper than the proposed functional form. This may be due to the small system sizes that are available numerically.

In **Figure 8**, we show the results of the analysis of the temporal velocity distribution. Again, we attempt to fit the data to a power law with exponential cutoff,

$$G(\Delta t) = B \left( \frac{\Delta t}{t^*} \right)^{-\tau_t} \exp \left( -\frac{\Delta t}{t^*} \right), \quad (20)$$

with  $t^* = 0.25/\langle v \rangle$  and exponent  $\tau_t = 0.43$ . This functional form was proposed by Tallakstad et al. [13], including the value  $\tau_t = 0.43$ .

We note that the prefactor  $A$  in Equation (19) is, according to **Figure 7**, proportional to  $\sqrt{g}$ , where  $g$  is the gradient in the threshold distribution. Likewise, the prefactor  $B$  in Equation (20) is, according to **Figure 5**, proportional to  $g\sqrt{L}$ .

### 3.3. CLUSTER ANALYSIS

In the following we analyze the geometrical structure of the areas swept by the crack front during avalanches. We denote such an area a *cluster*. Also here we use values of  $e$ .

Tallakstad et al. [13] define a *pinning* regime where  $v < \langle v \rangle$  and a *depinning* regime where  $v > \langle v \rangle$ . As they did, we construct

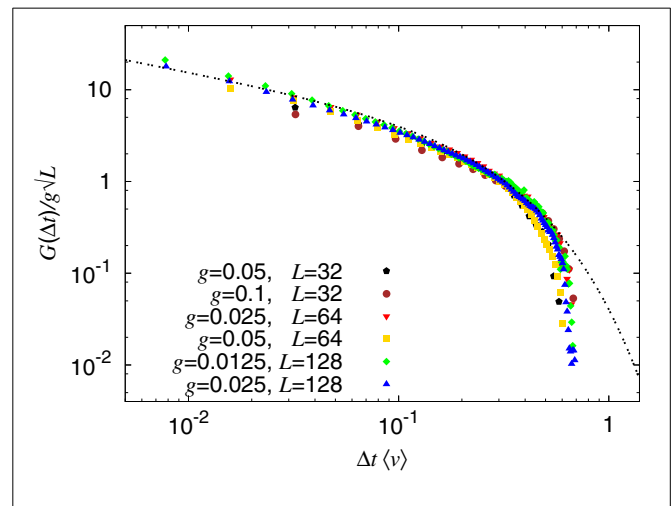


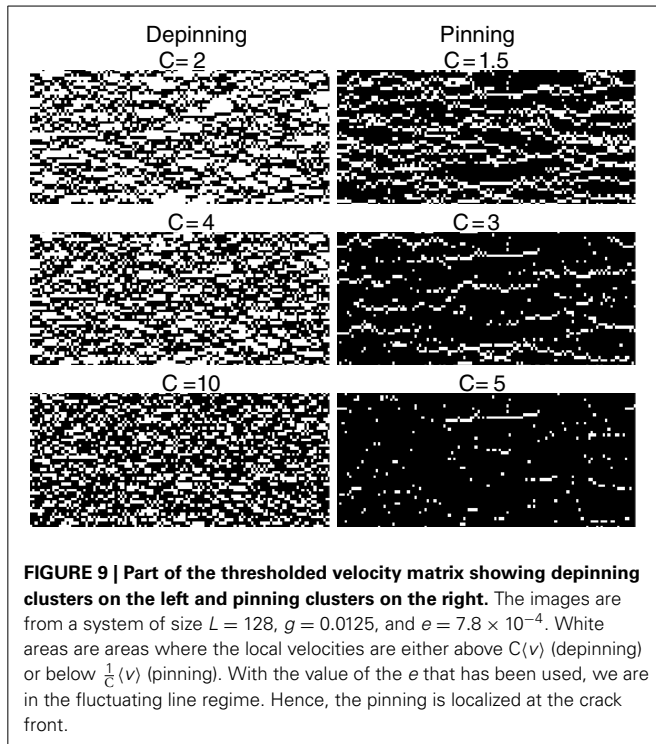
**FIGURE 8 | Temporal correlation function  $D(\Delta t)$ .** Best data collapse is obtained when scaling  $\Delta t$  by  $1/\langle v \rangle$  and  $G(\Delta t)$  by  $\langle v \rangle^{0.43} g\sqrt{L}$ . The line is a fit to a power law with exponential cutoff  $G(\Delta t) = B(\Delta t/\langle v \rangle)^{-0.43} \exp(-\Delta t/\langle v \rangle/0.25)$ . The system sizes and elastic constant used are as in **Figure 6**.

thresholded velocity maps  $V_C$  in such a way that

$$V_C = \begin{cases} 1, & \text{for } v \geq C\langle v \rangle \\ 0, & \text{for } v < C\langle v \rangle \end{cases}, \quad (21)$$

in the depinning regime and

$$V_C = \begin{cases} 1, & \text{for } v \leq \langle v \rangle/C \\ 0, & \text{for } v > \langle v \rangle/C \end{cases}, \quad (22)$$

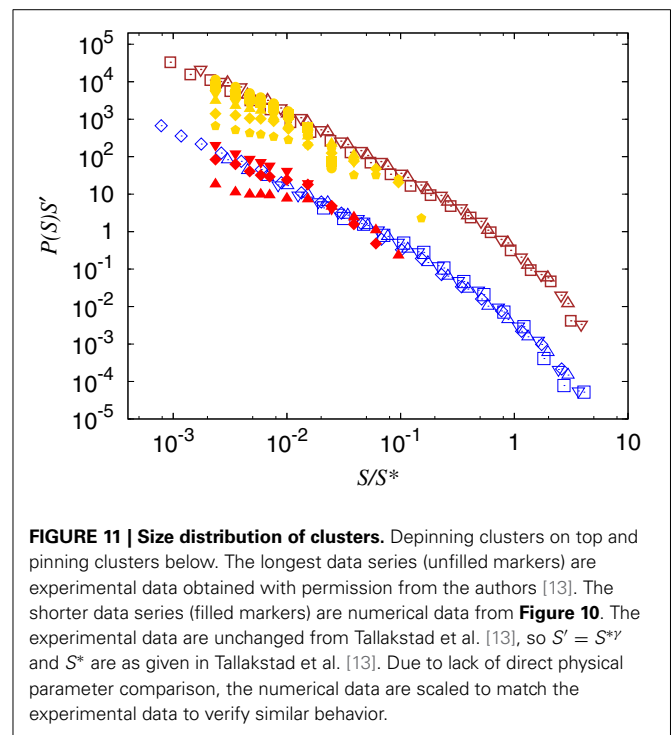
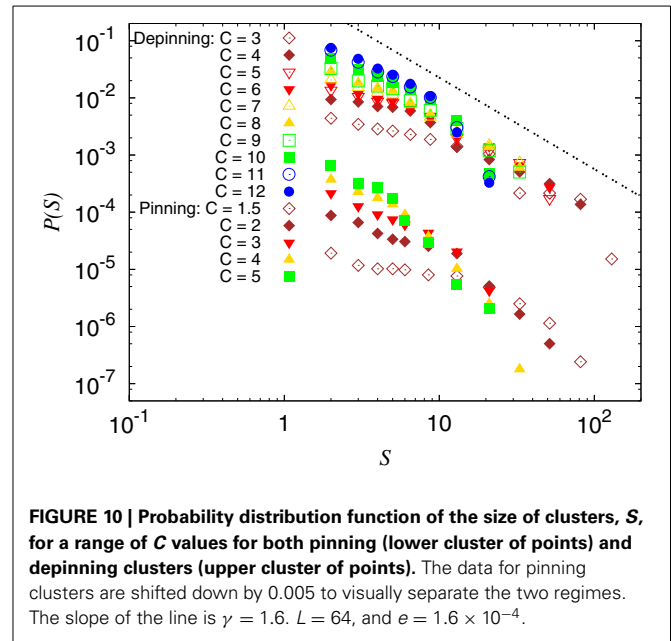


in the pinning regime.  $C$  is a constant in the range of 2–12 for depinning and 1.5 – 6 for pinning for our simulations. For larger system sizes, larger  $C$  are possible. Examples of these matrices are shown in **Figure 9**, where the structural difference between depinning and pinning clusters can be seen. In the spirit of de Saint-Exupéry we may characterize the pinning clusters as “snakelike,” whereas the depinning clusters are “elephant-in-snakelike” [40]. The following analysis uses only  $L = 64$  and  $L = 128$ , and are based on 250 and 100 samples, respectively.  $g = 0.025$  for the smaller systems, and  $g = 0.0125$  for the larger systems. For  $L = 64$ ,  $e = 1.6 \times 10^{-4}$ , and for  $L = 128$ ,  $e = 7.8 \times 10^{-4}$ . The systems will for these  $e$ -values behave virtually identical [22].

### 3.3.1. Size distribution of clusters

We denote the number of fibers in a cluster the area of the cluster  $S$ . Both experiments [12, 13] and numerical simulations using the fluctuating line model [17] on in-plane fracture, show a power law distribution  $P(S) \sim S^{-\gamma}$  for  $S$  with exponent close to  $\gamma = 1.56$  [13] or  $\gamma = 1.65$  [17].

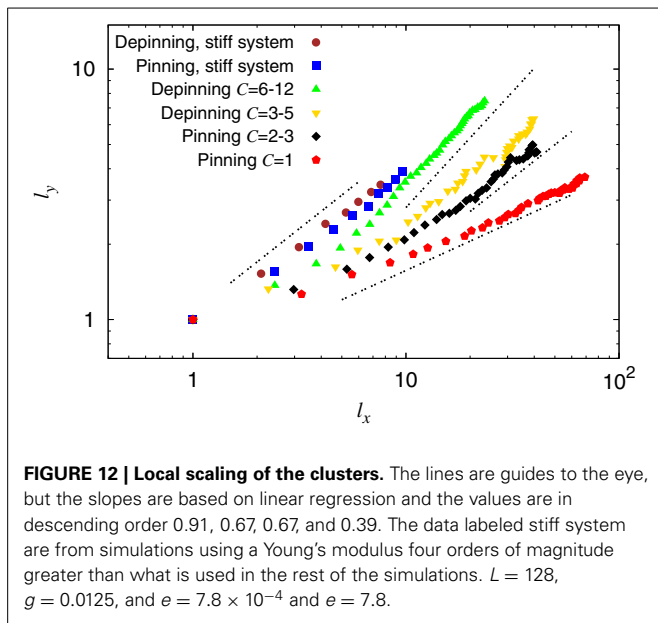
We show in **Figure 10** the probability distribution of  $S$  both for pinning and depinning for scaled elastic constant  $e = 1.6 \times 10^{-4}$ . Our data is consistent with previous measurements, but due to the limited size of the numerical simulations currently available, the exponent cannot be accurately determined. One prominent feature of the clusters is that due to the small system size, the presence of large clusters for low values of  $C$  suppresses the number of smaller clusters, and for high values of  $C$ , the number of large clusters is reduced by the filtering process in  $C$ . This is a pure finite size effect. The experiments, which would correspond to a very large simulation size, shows no such dependence on  $C$ . A direct



comparison between the experimental and our data is given in **Figure 11**.

### 3.3.2. Aspect ratio of clusters

Next, we extract the linear extensions of the clusters in the growth direction and orthogonally to it. This is done by enclosing each cluster in a bounding box of size  $l_x$  by  $l_y$ . Although the appearance differs greatly between pinning and depinning clusters, the method for determining  $l_x$  and  $l_y$  are the same.



We now turn to examining the relation between  $l_y$  and  $l_x$ . We plot these against each other in **Figure 12**. This data is more well-behaved than the probability distributions, so scaling relations are more pronounced. The data are consistent with a relation of type

$$l_y \sim l_x^H, \quad (23)$$

as studied both by Tallakstad et al. [13] and Bonamy et al. [17] in, respectively, the experimental system and numerically using the fluctuating line model.

We see a clear dependency of  $H$  on parameters such as  $e$  and  $C$ . Considering the depinning case first for  $e = 7.8 \times 10^{-4}$ , we divide the data between  $C^{\text{high}} \in [6 - 12]$ , a group containing data from only the highest local velocities, and  $C^{\text{low}} \in [3 - 5]$ , containing lower local velocities. There is a clear visual difference in behavior between the two groups: The group with the higher  $C$  values, have the higher slope. We measure the corresponding exponents to be  $H_d^{\text{high}} = 0.9$  and  $H_d^{\text{low}} = 0.65$ .

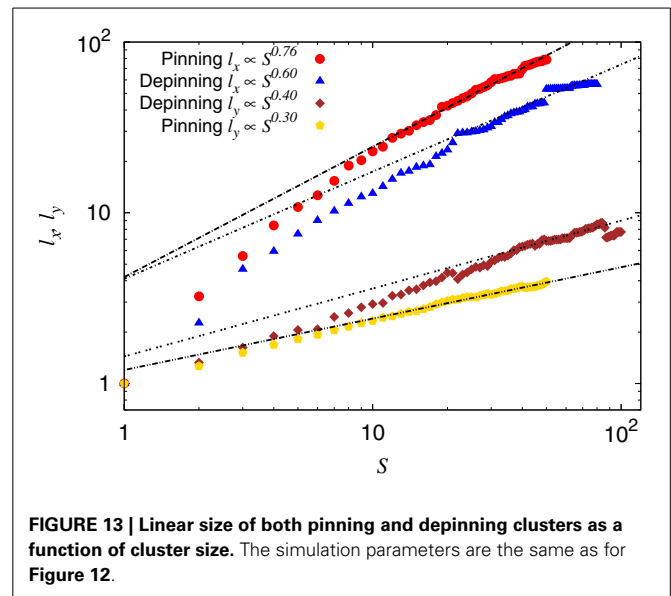
In the pinning regime we similarly divide between low and high local velocity effects, except that the range of available  $C$  is much smaller, so we find  $C^{\text{high}} = 2, 3$  and  $C^{\text{low}} = 1$ . This yields the two exponents  $H_p^{\text{high}} = 0.65$  and  $H_p^{\text{low}} = 0.4$ .

It has been suggested that  $H$  is another measure of the roughness exponent defined in Equation (11),  $\zeta$  [12, 16, 17]. In order to test this, we have added data both for pinning and depinning of a stiff system ( $e = 7.8$ ) in **Figure 12**. If the conjecture is right in this case, we would expect a  $H$  exponent equal to  $2/3$ . We have added such slopes, and the result is consistent with this conjecture.

Another way to examine these scaling relations is to check the relation between  $l_x$ ,  $l_y$  and  $S$ . We expect to see a power law relationship of type

$$l_i \sim S^{\alpha_i}, \quad (24)$$

since the size of the clusters are related through power laws. The data are plotted in **Figure 13**, in which data for the highest local



velocities are not included,  $C = C^{\text{low}}$  for both pinning and depinning. In the depinning regime, we find the exponents  $\alpha_x^d = 0.6$  and  $\alpha_y^d = 0.4$ . Eliminating  $S$ , we get a measure of  $H$  through

$$l_y \sim l_x^{\alpha_y/\alpha_x} = l_x^H, \quad (25)$$

resulting in  $H_d = 0.65$ . In the pinning regime we find  $\alpha_x^p = 0.75$  and  $\alpha_y^p = 0.3$ , yielding  $H_p = 0.4$ .

These results are to be compared to the experimental measurements of Tallakstad et al. [13] giving  $\alpha_x = 0.62 \pm 0.04$  in pinning and the depinning regime and  $\alpha_y = 0.41 \pm 0.06$  or  $0.34 \pm 0.05$  in the depinning regime depending on how the bounding box was defined. This leads to the value  $H = \alpha_y/\alpha_x = 0.66$  or  $0.55$  depending on the bounding box used. Bonamy et al. [17] found  $H = 0.65 \pm 0.05$  numerically using the fluctuating line model.

#### 4. DISCUSSION AND CONCLUSION

We have studied the fracture front in the soft clamp fiber bundle model when a gradient in the threshold distribution is introduced. The rescaled elastic constant  $e$  and the threshold gradient  $g$  are the most important input parameters in the model.  $g$  effectively controls the loading conditions and mimicks the plying apart of the two sintered PMMA plates in the experiment of Tallakstad et al. [13]. A high value for  $g$  amounts to a large angle of contact between the materials, or slow loading conditions, and vice versa. As long as  $1/g$  is in a range where it allows the front to develop but not extend out of the system, we see no change in any scaling exponents we have investigated when  $g$  is changed. This behavior echoes the experimental study where no dependence on the loading conditions was found and the average propagation velocity of the front spanned more than four and a half orders of magnitude [13].

The parameter  $e$ , defined in Equation (3), controls the material behavior. A small value for  $e$  may model a system of low modulus of elasticity, but also a system at long length scales. Likewise, a



**Table 1 | Comparison between the exponents measured in the work and those found experimentally.**

Exponent	This work	Experiment
$\zeta_+$	0.39(4)	0.35(5) [8]
$\zeta_-$	$2/3 \approx 0.667$	0.60(5) [8]
$\kappa_+$	0.75(7)	
$\kappa_-$	$637/432 \approx 1.47$	
$\kappa$		1.2 [11]
$\tau_x$	$\approx 0.4$	0.53(12) [13]
$\eta$	$\approx 2.53$	2.55(15) [13]
$\delta_+$	0.52(5)	
$\delta_-$	$288/637 \approx 0.45$	
$\delta$		$\approx 0.55$ [13]
$\delta$		$\approx 0.52$ [18]

Exponents indicated with subscripts “+” or “-” refer to large-scale or small-scale values. Exponents without subscripts reported from this work have all been measured in the large-scale regime. Exponents without subscripts reported by others (in the third column) have been measured without a distinction between small and large scales.

large  $e$  may model a system of large elastic modulus, but also a system at small length scales. We have in this paper associated the different  $e$  values we have studied with the scales at which we study the system.

A number of scaling exponents have been measured and compared to their experimental counterparts. We summarize the most important in **Table 1**.

In Section 3.3.2 we discussed shape of the clusters defined through the avalanches. The following picture emerges: For low values of  $e$ , the fracture process is due to stress concentration leading to damage forming on the fracture front. This regime is classified by a roughness exponent of  $\zeta_+ = 0.39 \pm 0.04$ . By studying the shape of the clusters defined through the avalanche dynamics, we find the same value for  $H$ . As  $e$  increases—corresponding to decreasing the length scale at which the system is observed—the clusters formed by the avalanche process changes shape and are now characterized by an exponent  $H = \zeta_- = 0.67$ , while the fracture front itself is still characterized by  $\zeta_+$ . As  $e$  is increased further, damage begins to form ahead of the front, and the front now grows due to damage coalescence. At this point, the roughness exponent changes from 0.39 and grows into 0.67. At higher  $e$ , both the burst process and the roughness of the front is now characterized by the larger exponent  $H = \zeta_- = 0.67$ .

## ACKNOWLEDGMENTS

We are grateful for discussions and suggestions by D. Bonamy, K. J. Måløy, L. Ponson, J. Schmittbuhl, and K. T. Tallakstad. This work was supported by the Norwegian Research Council (NFR) under grant number 177591/V30. Part of this work made use of the facilities of HECToR, the UK’s national high performance computing service, which is provided by UoE HPCx Ltd at the University of Edinburgh, Cray Inc and NAG Ltd, and funded by the Office of Science and Technology through EPSRC’s High End Computing Programme.

## REFERENCES

- Lawn BR. *Fracture of Brittle Solids, 2nd Edn*. Cambridge: Cambridge University Press (1993). doi: 10.1017/CBO9780511623127
- Schmittbuhl J, Roux S, Vilotte JP, Måløy KJ. Interfacial crack pinning: effect of nonlocal interactions. *Phys Rev Lett*. (1995) **74**:1787. doi: 10.1103/PhysRevLett.74.1787
- Schmittbuhl J, Måløy KJ. Direct observation of a self-affine crack propagation. *Phys Rev Lett*. (1997) **78**:3888. doi: 10.1103/PhysRevLett.78.3888
- Ramanathan S, Ertas D, Fisher DS. Quasistatic crack propagation in heterogeneous media. *Phys Rev Lett*. (1997) **79**:873. doi: 10.1103/PhysRevLett.79.873
- Delaplace A, Schmittbuhl J, Måløy KJ. High resolution description of a crack front in a heterogeneous Plexiglas block. *Phys Rev E* (1999) **60**:1337. doi: 10.1103/PhysRevE.60.1337
- Rosso A, Krauth W. Roughness at the depinning threshold for a long-range elastic string. *Phys Rev E* (2002) **65**:025101(R). doi: 10.1103/PhysRevE.65.025101
- Schmittbuhl J, Hansen A, Batrouni GG. Roughness of interfacial crack fronts: stress-weighted percolation in the damage zone. *Phys Rev Lett*. (2003) **90**:045505. doi: 10.1103/PhysRevLett.90.045505
- Santucci S, Grob M, Toussaint R, Schmittbuhl J, Hansen A, Måløy KJ. Fracture roughness scaling: a case study on planar cracks. *Europhys Lett*. (2010) **92**:44001. doi: 10.1209/0295-5075/92/44001
- Bonamy D. Intermittency and roughening in the failure of brittle heterogeneous materials. *J Appl Phys D* (2009) **42**:214014. doi: 10.1088/0022-3727/42/21/214014
- Bonamy D, Bouchaud E. Failure of heterogeneous materials: a dynamic phase transition? *Phys Rep*. (2011) **498**:1–44. doi: 10.1016/j.physrep.2010.07.006
- Måløy KJ, Schmittbuhl J. Dynamical events during slow crack propagation. *Phys Rev Lett*. (2001) **87**:105502. doi: 10.1103/PhysRevLett.87.105502
- Måløy KJ, Santucci S, Schmittbuhl J, Toussaint R. Local waiting time fluctuations along a randomly pinned crack front. *Phys Rev Lett*. (2006) **96**:045501. doi: 10.1103/PhysRevLett.96.045501
- Tallakstad KT, Toussaint R, Santucci S, Schmittbuhl J, Måløy KJ. Local dynamics of a randomly pinned crack front during creep and forced propagation: an experimental study. *Phys Rev E* (2011) **83**:046108. doi: 10.1103/PhysRevE.83.046108
- Lengliné O, Toussaint R, Schmittbuhl JE, Ampuero JP, Tallakstad KT, Santucci S, et al. Average crack-front velocity during subcritical fracture propagation in a heterogeneous medium. *Phys Rev E* (2011) **84**:036104. doi: 10.1103/PhysRevE.84.036104
- Bouchaud JP, Bouchaud E, Lapasset G, Planès J. Models of fractal cracks. *Phys Rev Lett*. (1993) **71**:2240. doi: 10.1103/PhysRevLett.71.2240
- Laurson L, Santucci S, Zapperi S. Avalanches and clusters in planar crack front propagation. *Phys Rev E* (2010) **81**:046116. doi: 10.1103/PhysRevE.81.046116
- Bonamy D, Santucci S, Ponson L. Crackling dynamics in material failure as the signature of a self-organized dynamic phase transition. *Phys Rev Lett*. (2008) **101**:045501. doi: 10.1103/PhysRevLett.101.045501
- Sethna J, Dahmen K, Myers C. Crackling noise. *Nature* (2001) **410**:242–250. doi: 10.1038/35065675
- Bouchaud E, Bouchaud JP, Fisher DS, Ramanathan S, Rice JR. Can crack front waves explain the roughness of cracks? *J Mech Phys Sol*. (2002) **50**:1703. doi: 10.1016/S0022-5096(01)00137-5
- Batrouni GG, Hansen A, Schmittbuhl J. Heterogeneous interfacial failure between two elastic blocks. *Phys Rev E* (2002) **65**:036126. doi: 10.1103/PhysRevE.65.036126
- Gjerden KS, Stormo A, Hansen A. A model for stable interfacial crack growth. *J Phys Conf Series* (2012) **402**:012039. doi: 10.1088/1742-6596/402/1/012039
- Gjerden KS, Stormo A, Hansen A. Universality classes in constrained crack growth. *Phys Rev Lett*. (2013) **111**:135502. doi: 10.1103/PhysRevLett.111.135502
- Sapoval B, Rosso M, Gouyet JF. The fractal nature of a diffusion front and the relation to percolation. *J Phys Lett*. (1985) **46**:149–156. doi: 10.1051/jphyslet:01985004604014900
- Gouyet JF, Rosso M. Diffusion fronts and gradient percolation: a survey. *Physica A* (2005) **357**:86–96. doi: 10.1016/j.physa.2005.05.054
- Hansen A, Batrouni GG, Ramstad T, Schmittbuhl J. Self-affinity in the gradient percolation problem. *Phys Rev E* (2007) **75**:030102. doi: 10.1103/PhysRevE.75.030102

26. Mehrabi AR, Rassamdana H, Sahimi M. Characterization of long-range correlations in complex distributions and profiles. *Phys Rev E* (1997) **56**:712. doi: 10.1103/PhysRevE.56.712
27. Simonsen I, Hansen A, Nes OM. Determination of the Hurst exponent by use of wavelet transforms. *Phys Rev E* (1998) **58**:2779. doi: 10.1103/PhysRevE.58.2779
28. Pradhan S, Hansen A, Chakrabarti BK. Failure processes in elastic fiber bundles. *Rev Mod Phys.* (2010) **82**:499. doi: 10.1103/RevModPhys.82.499
29. Johnson KL. *Contact Mechanics*. Cambridge: Cambridge University Press (1985). doi: 10.1017/CBO9781139171731
30. Batrouni GG, Hansen A, Nelkin M. Fourier acceleration of relaxation processes in disordered systems. *Phys Rev Lett.* (1986) **57**:1336. doi: 10.1103/PhysRevLett.57.1336
31. Batrouni GG, Hansen A. Fourier acceleration of iterative processes in disordered systems. *J Stat Phys.* (1988) **52**:747–773. doi: 10.1007/BF01019728
32. Stormo A, Gjerden KS, Hansen A. Onset of localization in heterogeneous interfacial failure. *Phys Rev E* (2012) **86**:025101(R). doi: 10.1103/PhysRevE.86.025101
33. Hansen A. Physics and fracture. *Comp Sci Engn.* (2005) **7**:90. doi: 10.1109/MCSE.2005.99
34. Delaplace A, Roux S, Pijaudier-Cabot G. Avalanche statistics of interface crack propagation in fiber bundle model: characterization of cohesive crack. *J Engn Mech.* (2001) **127**:646–652. doi: 10.1061/(ASCE)0733-9399(2001)127:7(646)
35. Stauffer D, Aharony A. *Introduction to Percolation Theory*. London: Francis and Taylor (1992).
36. Family F, Vicsek T. Scaling of the active zone in the Eden process on percolation networks and the ballistic deposition model. *J Phys A* (1985) **18**:L75. doi: 10.1088/0305-4470/18/2/005
37. Mandelbrot BB. *Fractal Forms, Chance and Dimensions*. San Francisco, CA: W. H. Freeman (1977).
38. Schmittbuhl J, Delaplace A, Måløy KJ. *Physical Aspects of Fracture*, eds E. Bouchaud, D. Jeulin, C. Prioul, S. Roux (Amsterdam: Kluwer Academic Publishers) (2001).
39. Duemmer O, Krauth W. Depinning exponents of the driven long-range elastic string. *J Stat Mech.* **2007**:P01019 (2007). doi: 10.1088/1742-5468/2007/01/P01019
40. de Saint-Exupéry, A. *Le Petit Prince*. Paris: Éditions Gallimard (1943).

**Conflict of Interest Statement:** The authors declare that the research was conducted in the absence of any commercial or financial relationships that could be construed as a potential conflict of interest.

Received: 21 August 2014; paper pending published: 15 October 2014; accepted: 01 November 2014; published online: 20 November 2014.

Citation: Gjerden KS, Stormo A and Hansen A (2014) Local dynamics of a randomly pinned crack front: a numerical study. *Front. Phys.* **2**:66. doi: 10.3389/fphy.2014.00066

This article was submitted to *Interdisciplinary Physics*, a section of the journal *Frontiers in Physics*.

Copyright © 2014 Gjerden, Stormo and Hansen. This is an open-access article distributed under the terms of the Creative Commons Attribution License (CC BY). The use, distribution or reproduction in other forums is permitted, provided the original author(s) or licensor are credited and that the original publication in this journal is cited, in accordance with accepted academic practice. No use, distribution or reproduction is permitted which does not comply with these terms.